The Astrophysical Journal, 694:1619–1628, 2009 April 1 doi:10.1088/0004-637X/694/2/1619

ARRAY FOR MICROWAVE BACKGROUND ANISOTROPY: OBSERVATIONS, DATA ANALYSIS, AND RESULTS FOR SUNYAEV–ZEL'DOVICH EFFECTS

Jiun-Huei Proty Wu[1,2], Paul T. P. Ho[3,4], Chih-Wei Locutus Huang[1,2], Patrick M. Koch[3], Yu-Wei Liao[1,2], Kai-Yang Lin[1,3], Guo-Chin Liu[3,5], Sandor M. Molnar[3], Hiroaki Nishioka[3], Keiichi Umetsu[2,3], Fu-Cheng Wang[1,2], Pablo Altamirano[3], Mark Birkinshaw[6], Chia-Hao Chang[3], Shu-Hao Chang[3], Su-Wei Chang[3], Ming-Tang Chen[3], Tzihong Chiueh[1,2], Chih-Chiang Han[3], Yau-De Huang[3], Yuh-Jing Hwang[3], Homin Jiang[3], Michael Kesteven[7], Derek Y. Kubo[3], Katy Lancaster[6], Chao-Te Li[3], Pierre Martin-Cocher[3], Peter Oshiro[3], Philippe Raffin[3], Tashun Wei[3], and Warwick Wilson[7]

[1] Department of Physics, Institute of Astrophysics, & Center for Theoretical Sciences, National Taiwan University, Taipei 10617, Taiwan
[2] LeCosPA Center, National Taiwan University, Taipei 10617, Taiwan
[3] Institute of Astronomy and Astrophysics, Academia Sinica, P.O. Box 23-141, Taipei 10617, Taiwan
[4] Harvard-Smithsonian Center for Astrophysics, 60 Garden Street, Cambridge, MA 02138, USA
[5] Department of Physics, Tamkang University, 251-37 Tamsui, Taipei County, Taiwan
[6] University of Bristol, Tyndall Avenue, Bristol BS8 1TL, UK
[7] Australia Telescope National Facility, P.O. Box 76, Epping, NSW 1710, Australia
Received 2008 October 10; accepted 2009 February 6; published 2009 March 25

ABSTRACT

We present observations, analysis, and results for the first-year operation of Array for Microwave Background Anisotropy (AMiBA), an interferometric experiment designed to study cosmology via the measurement of cosmic microwave background (CMB). AMiBA is the first CMB interferometer operating at 3 mm to have reported successful results, currently with seven close-packed antennas of 60 cm diameter giving a synthesized resolution of around 6′. During 2007, AMiBA detected the Sunyaev–Zel'dovich effects (SZEs) of six galaxy clusters at redshift $0.091 \leqslant z \leqslant 0.322$. An observing strategy with on–off-source switching is used to minimize the effects from electronic offset and ground pickup. Planets were used to test the observational capability of AMiBA and to calibrate the conversion from correlator time-lag data to visibilities. The detailed formalism for data analysis is given. We summarize our early tests including observations of planets and quasars, and present images, visibility profiles, the estimated central coordinates, sizes, and SZE amplitudes of the galaxy clusters. Scientific implications are summarized. We also discuss possible systematic effects in the results.

Key words: cosmic microwave background – cosmology: observations – galaxies: clusters: general – methods: data analysis

1. INTRODUCTION

The cosmic microwave background (CMB) has been used as a window through which to study not only the early universe but also its evolutionary history. The challenge of such observations arises from the fact that the CMB carries information spanning a period of about 14 billion years, so that specially designed instruments and analysis methods are required to separate the effects originated from different physical processes. One recent focus is the measurement of the Sunyaev–Zel'dovich effects (SZEs) resulting from the hot gas in galaxy clusters (Sunyaev & Zeldovich 1972; Birkinshaw & Lancaster 2007). Several CMB experiments are dedicated to this purpose, such as ACT (Kosowsky 2003), AMI (Kneissl et al. 2001), APEX-SZ (Halverson et al. 2008), Owens Valley Radio Observatory (OVRO)/Berkeley–Illinois–Maryland Association (BIMA)-SZE (LaRoque 2006), SPT (Ruhl et al. 2004), SZA (Muchovej et al. 2007), and OCRA-p (Lancaster et al. 2007). Here, we report the first results of SZE observations with the Y. T. Lee Array for Microwave Background Anisotropy (AMiBA; Ho et al. 2009).

AMiBA is devoted to CMB observation with particular emphasis on detecting SZE clusters, the CMB anisotropy, and possibly cosmic defects (Lin et al. 2004; Umetsu et al. 2004; Wu et al. 2004, 2008; Ho et al. 2008). The instrument is described in Ho et al. (2009), Chen et al. (2009), and Koch et al. (2009a). In our initial configuration with seven close-packed antennas of 60 cm diameter, we concentrated on pointed observations of the SZE and the measurement of the CMB temperature power spectrum (Ho et al. 2008; Wu et al. 2008).

At the AMiBA operating frequency (86–102 GHz; ∼ 3 mm wavelength) the SZE is expected to induce a decrement in the CMB intensity as compared with the undistorted Planckian spectrum (see Section 2). This provides a powerful tool for discriminating between galaxy clusters and other astronomical sources, because the latter normally emit photons characteristic of much harder spectra than the CMB, and therefore always induce an increment in intensity rather than a decrement. By measuring the SZE intensity deficit and its profile, we hope to probe not only the cluster physics but also the related cosmic origins.

This paper is organized as follows. In Section 2, we describe the AMiBA telescope and its relation to the SZE. In Section 3, we summarize our initial observations in 2007 with emphasis on the observing strategy and target selection. In Section 4, we describe our analysis formalism and procedures for obtaining the calibrated visibilities from the raw time-lag data, and the SZE images and profiles from the calibrated visibilities. The main results are also presented here. In Section 5, we discuss possible systematic errors. In Section 6, we summarize the scientific implications of these results, including the estimation of Hubble constant (Koch et al. 2009b), the scaling relationship between the SZE and X-ray-derived properties (Huang et al. 2009), and the baryonic fraction when our SZE data are jointly analyzed

with the Subaru lensing data (Umetsu et al. 2009). Brief conclusions are given in Section 7. We have other companion papers investigating the system performance (Lin et al. 2009), the foreground (Liu et al. 2009), and data integrity (Nishioka et al. 2009).

2. AMiBA TELESCOPE AND SZE

AMiBA is an interferometric experiment initiated in Taiwan in 2000 and dedicated on Mauna-Loa (3400 m in elevation), Big Island, Hawaii on 2006 October 3. It has dual-channel receivers operating at 86–102 GHz, designed to have full polarization capabilities (Chen et al. 2009). Currently, it has seven close-packed Cassegrain antennas of 60 cm diameter (Koch et al. 2006) giving a synthesized resolution of 6 arcmin (see Section 3.2), expandable to a total of 19 elements with a synthesized resolution of about 2 arcmin. The project has been funded for an expansion to 13 elements with dishes of 1.2 m diameter. The 13-element system is expected to start operating in the early 2009. Its capability in studying the SZE science is investigated by Molnar et al. (2009, in preparation).

The receiver-antenna elements are reconfigurable and co-mounted on a 6 m platform, which is driven by a hexapod mount (Koch et al. 2009a). Each element has a cooled heterodyne receiver, consisting of HEMT amplifiers of 46 dB in amplification, subharmonic mixers, and 2–18 GHz IF amplifiers. For each baseline, the signals from two dual-channel receivers are cross-correlated in an analog four-lag correlator, whose time-lag outputs are convertible to two complex visibilities corresponding to the upper and lower frequency bands (see Section 4). The cross-correlation between the L and R polarization modes (the dual channels) of a pair of receivers enables the measurement of the four Stokes parameters, T, Q, U, and V. Currently, AMiBA operates with only two cross-polarization modes of LL and RR, focusing on the measurement of T. The typical receiver noise temperatures are between 80 and 110 K (Lin et al. 2009).

In 2007, the seven-element AMiBA focuses on targeted SZE observations. The theoretically expected SZE in the flux density is

$$\Delta I_{\rm SZE}(f) = \Delta I_{\rm tSZE}(f, y) + \Delta I_{\rm kSZE}(f, \tau, v_{\rm p}), \quad (1)$$

where $\Delta I_{\rm tSZE}$ and $\Delta I_{\rm kSZE}$ are the thermal and kinematic SZE, respectively, defined as

$$\Delta I_{\rm tSZE}(f, y) = I_0 y\,[g(x) + \delta_{\rm rel}(f, T_{\rm e})]\,, \quad (2)$$

$$\Delta I_{\rm kSZE}(f, \tau, v_{\rm p}) = -I_0 \beta \tau h(x). \quad (3)$$

Here f is the observing frequency, $I_0 = 2(kT_{\rm CMB})^3/(hc)^2 \approx 2.7 \times 10^8$ Jy Sr^{-1} for a CMB temperature of $T_{\rm CMB} = 2.725$ K, $y = k\sigma_{\rm T}/(m_{\rm e}c^2)\int T_{\rm e} n_{\rm e} dl$ is the Compton parameter, $g(x) = h(x)[x/\tanh(x/2) - 4]$ with $x = hf/(kT_{\rm CMB})$, $\delta_{\rm rel}$ is a relativistic correction, $\beta = v_{\rm p}/c$ is the peculiar radial velocity in units of the speed of light, $\tau = \sigma_{\rm T}\int n_{\rm e} dl$ is the optical depth, $h(x) = x^4 e^x/(e^x - 1)^2$, c is the speed of light, $m_{\rm e}$ is the electron mass, $n_{\rm e}$ is the electron number density in the cluster, $T_{\rm e}$ is the electron temperature, k is the Boltzmann constant, h is the Planck constant, and $\sigma_{\rm T}$ is the Thomson cross section.

For the thermal effects, the $\Delta I_{\rm tSZE}$ has a maximum decrement with respect to the CMB Planckian spectrum $I_{\rm CMB}(f) = I_0 x^3/(e^x - 1)$ at $f \approx 100$ GHz. This optimal frequency for SZE observations is well covered by the AMiBA operating frequency of $f = [86, 102]$ GHz. For AMiBA $g(f) \approx -3.4$ at the center frequency $f = 94$ GHz, with a variation of less than $\pm 10\%$ for the range of [86, 102] GHz. Therefore for a typical massive cluster with $y \sim 10^{-4}$, $T_{\rm e} \sim 10$ keV, $\tau \sim y m_{\rm e}c^2/(kT_{\rm e}) \approx 5 \times 10^{-3}$, $v_{\rm p} = 1000$ km s^{-1}, and an angular size of $\theta = 6'$, we expect the SZE signals to be $\Delta I_{\rm tSZE}\pi(\theta/2)^2 \sim -200$ mJy and $|\Delta I_{\rm kSZE}|\pi(\theta/2)^2 \sim 20$ mJy for AMiBA, indicating $|\Delta I_{\rm kSZE}/\Delta I_{\rm tSZE}| \approx 10\%$. The fractional contribution from the relativistic correction $\delta_{\rm rel}$ in such a case is about 7%. Thus, we expect the AMiBA SZE signals to be dominated by the thermal effects, with a feature of decrement in the flux density. We also note that $|I_{\rm CMB}(94\ {\rm GHz})| \approx 2.9 \times 10^8$ Jy Sr^{-1}, so that $|\Delta I_{\rm tSZE}/I_{\rm CMB}| \approx 3 \times 10^{-4}$.

The operating frequency of [86, 102] GHz also has the advantage that the SZE signals are less affected by the point sources when compared with the observations at a lower frequency, which is more typical for interferometric experiments such as AMI (15 GHz; Kneissl et al. 2001), SZA (27–35 GHz; Muchovej et al. 2007), and OVRO/BIMA (30 GHz; Reese et al. 2002). This is because typically the point sources have power-law spectra of flux density with negative spectral indices, so that they contribute less toward higher frequencies. We note that although SZA also has instruments at 90–98 GHz, their baselines are about 10 times longer than ours providing information at much smaller angular scales that is complementary to what AMiBA can supply. Another advantage of the AMiBA frequency range is that it also suppresses the Galactic synchrotron radiation and dust emission. Detailed investigation about the AMiBA foreground is presented in Liu et al. (2009). These features in frequency and resolution make AMiBA a unique CMB telescope, complementing the capability of other CMB projects.

3. OBSERVATIONS

3.1. Primary Beams

Before the 60 cm antennas were mounted onto the platform, their beam patterns were individually measured in the far field (∼100 m) by scanning a wide-band white source with a system retrofitted from a commercial equatorial mount (Koch et al. 2006). Figure 1(a) shows an example. An azimuthal average of the beam pattern (Figure 1(b)) reveals a full width at half-maximum (FWHM) of about 23 arcmin. The first side lobe is about 20 db below the primary peak and the beam profile is as per designed. The index of asymmetry (Wu et al. 2001) is calculated showing that the discrepancy of the beam pattern from its azimuthal average is below 10% within the FWHM. All beam patterns of the antennas are well fitted by a Gaussian beam of 23 arcmin within the 2σ region for <10% error.

3.2. u–v Coverage and Resolution

In 2007, AMiBA was used with the seven 57.6 cm diameter antennas close-packed on the platform, providing 21 baselines of three different lengths $L^b = 60.6$, 105.0, and 121.2 cm. Each baseline operates at two frequency channels centered at $f = 90$ and 98 GHz, each with a bandwidth of 8 GHz. Thus, the three baseline lengths correspond to six multipole bands $\ell = 2\pi\sqrt{u^2 + v^2} = 2\pi L^b f/c = [1092, 1193]$, [1193, 1295], [1891, 2067], [2067, 2243], [2184, 2387], [2387, 2590]. These baselines have a sixfold symmetry (Ho et al. 2009). To achieve better u–v coverage and thus a better imaging capability, we observe each target at eight different polarization angles of the platform with an angular step of 7.°5, uniformly covering azimuthal angles in the u–v plane with 48 discrete samples for each of the three different baseline lengths at each of the

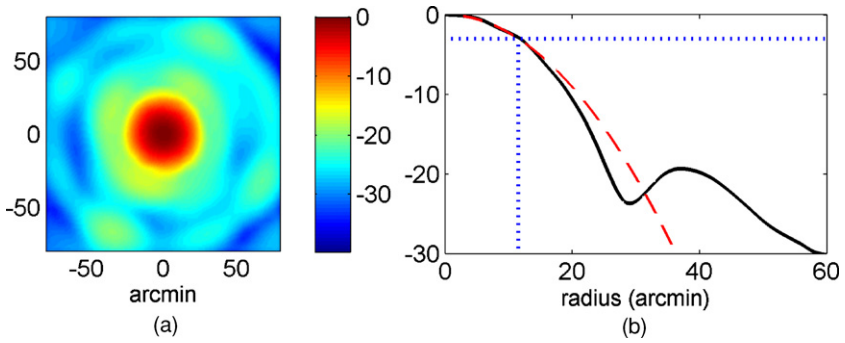

Figure 1. (a) Left: the measured primary beam of one of the 60 cm antennas. (b) Right: azimuthally averaged beam shape (solid) and a Gaussian fit (dashed); the dotted lines indicate the FWHM. In both plots the intensity is in units of db normalized to the peak value.

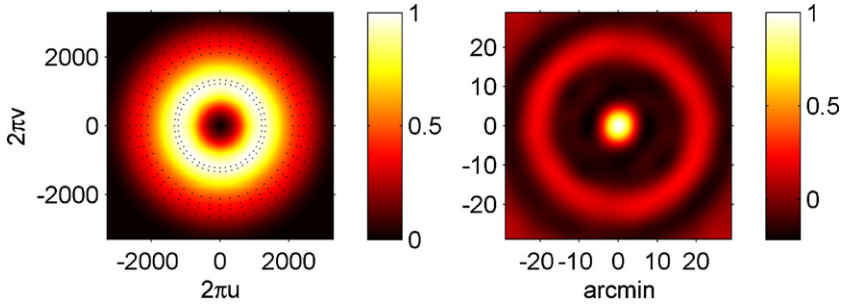

Figure 2. *u–v* coverage of a typical observation by seven-element AMiBA (left) and its corresponding noise-weighted synthesized beam (the dirty beam; right). In the left plot, the color scale indicates the relative sensitivity in *u–v* space, while the dots mark the *u–v* modes sampled by the typical AMiBA observation.

two frequency bands. This makes a total of 288 discrete *u–v* samples. Figure 2 shows such typical *u–v* coverage with the corresponding noise-weighted point-spread function from a typical observation, the so-called dirty beam. The FWHM of the dirty beam is about 6 arcmin, defining the synthesized resolution of the seven-element AMiBA. When using an equal-weighted (rather than the current noise-weighted) scheme to construct the dirty beam, we still obtain a similar resolution of about 6 arcmin because the noise level for each baseline is about the same.

3.3. Observing Strategy

To minimize, if not completely remove, the effects from ground pickup and from a DC component in the electronics that leaks into the data, we adopt a "two-patch" observing strategy that alternates between the target and a region of nominally blank sky. This strategy is similar to that used by CBI for the measurement of CMB polarization (Readhead et al. 2004).

In this mode, a leading patch that contains our target is tracked for 3 minutes, and then a trailing patch of the presumably blank sky is tracked for the same period of time. The trailing patch is located at an R.A. $3^{m}10^{s}$ greater than the R.A. of the target. Since it takes 10 s for the telescope to slew between the fields, the two patches are observed over identical azimuth and elevation tracks. During both tracks the platform polarization angle is controlled so that each baseline corresponds to a fixed *u–v* mode. The recorded data during the two tracks should then contain the same contribution from ground pickup, which is removed by a subsequent differencing of the two tracks. This strategy requires that both the electronic offset and the ground emission are stable within 6 minutes, which is far shorter as compared with the measured time dependence (Lin et al. 2009). The penalty for adopting such a two-patch strategy is the loss of efficiency by a factor of 4, where a factor of 2 comes from doubling the observing time and the other factor of 2 from doubling the noise variance when differencing the two patches. We also note that there is a CMB component as well as possible combinations from Galactic foreground and extragalactic point sources in the differencing map though at a level much lower than the expected SZE of massive clusters (Liu et al. 2009). Nevertheless before observations we did check our fields for such contaminations.

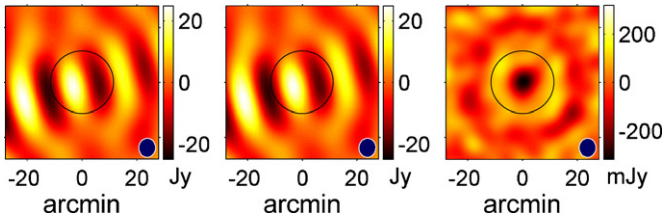

Figure 3. Modulation between the target (left) and the blank sky (center) successfully removes the strong contributions from ground pickup and electronic offset. The difference map (right) clearly reveals the signal from cluster A2142.

Figure 3 demonstrates the application of the two-patch observing strategy for SZE mapping. The left panel is an image constructed from the leading patch, containing cluster Abell 2142 (see Section 4 for the formalism and procedure of data analysis). The middle panel shows the corresponding image from the trailing patch of blank sky. It is clear that both patches are contaminated by signals much stronger than the SZE (mainly from the ground pickup), and that the images are closely similar. The difference of the two patches reveals the cluster signal (right panel), whose signal strength is only about 1% of the contamination signal in individual patches.

3.4. Calibration Events

To calibrate these data, we observe planets roughly every 3 hr using the same two-patch observing strategy. This time the two patches are each observed for 4 minutes and separated

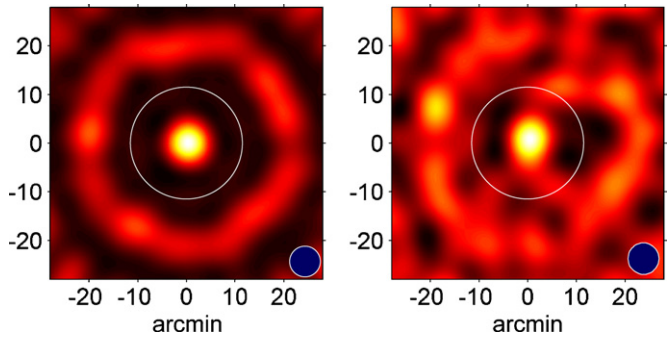

Figure 4. Dirty images of Saturn (left) and the quasar J0325+2224 (right), both calibrated by Jupiter using the formalism presented in Section 4.

by 4^m10^s in R.A. Such a separation in R.A. is equivalent to an angular separation of at least 57 arcmin, assuring that leakage of the planetary signal into the second patch is small, less than 0.1% of the planetary flux density according to the primary beam pattern measured in Section 3.1. The detailed formalism on how the data are converted to calibrated visibilities is presented in Section 4.3, and the determination of the planetary flux densities is discussed by Lin et al. (2009). Long-duration observations of the planets show that the system is stable at night (between about 8 p.m. and 8 a.m.) so that a planetary calibration every 3 hr controls the calibration error to be within 5% in gain and 0.1 radian in phase (Lin et al. 2009).

To test the overall performance of our observing, calibration, and analysis strategy, we first used the Sun to successfully phase calibrate an observation of Jupiter, and then Jupiter to phase and amplitude calibrate an observation of Saturn. The left plot of Figure 4 shows a dirty image of Saturn calibrated by an observation of Jupiter made 4 hr later. The FWHM of this image is identical to that of the dirty beam shown in Figure 2, and the index of asymmetry (Wu et al. 2001) of the cleaned image is well below 5%.

3.5. 2007 Observations and SZE Targets

After first light of the seven-element AMiBA in 2006 September, which was a drift scan on Jupiter and whose image was quickly constructed, several months of start-up tests were used to study the instrumental properties, to fine tune our system, to study the ground pickup, and to find an optimal observing strategy. During this period, Saturn, Mars, Venus, and the Crab Nebula were also observed for system tests. In 2007 February, when testing the two-patch observing strategy, we detected a first extragalactic object, quasar J0325 + 2224 with a total (unresolved) flux density of 550 mJy (the right plot of Figure 4).

After further fine tuning of the system, in 2007 April we detected our first SZE cluster, Abell 2142 with a central SZE decrement of around -320 mJy beam^{-1}. During 2007, we observed a total of six S–Z clusters with $0.091 \leqslant z \leqslant 0.322$: A1689, A1995, A2142, A2163, A2261, and A2390.

The observations were always at night time, when the system is stable. Due to the weather, system engineering, and observability of the targets, a total of roughly 150 observing hours was spent in observing the clusters or their trailing fields over a span of five months, from April to August in 2007. During this period a lot of efforts were dedicated to the system tests and tuning (Lin et al. 2009; Koch et al. 2009a). Table 1 summarizes the pointing directions, the observing and integration times, and the synthesized beam sizes, for each of the six clusters. Due to the two-patch observing strategy, which modulates between on- and off-source positions, the total time spent during cluster observations is double the on-cluster time listed in the table. The integration time on source ($t_{\rm int}$) is less than the actual observing time ($t_{\rm obs}$) because of the data trimming that will be discussed in Section 4.1.

Table 1
Observing Log for AMiBA SZE Clusters

Cluster	Pointing Directions (J2000)		$t_{\rm obs}$ (hr)	$t_{\rm int}$ (hr)	Synthesized Resolution
	R.A.	Decl.			
A1689	$13^h11.49^m$	$-1°20'.47$	8.75	7.11	6'.3
A1995	$14^h52.84^m$	$58°02'.80$	15.90	5.56	6'.6
A2142	$15^h58.34^m$	$27°13'.61$	7.05	5.18	6'.5
A2163	$16^h15.57^m$	$-6°07'.43$	7.80	6.49	6'.6
A2261	$17^h22.46^m$	$32°07'.62$	19.15	8.87	6'.4
A2390	$21^h53.61^m$	$17°41'.71$	16.05	11.02	6'.4

Notes. Observing log for the AMiBA observations of six clusters of galaxies, including the pointing directions, the observing ($t_{\rm obs}$) and integration ($t_{\rm int}$) times per baseline, and the synthesized resolution (syn. res.; the FWHM of the azimuthally averaged dirty beam).

The six clusters were chosen based on observational convenience, the expected flux density based on SZE observations at other frequencies, and the existence of extensive published X-ray data. The observational convenience requires that the targets can be seen at the Mauna-Loa latitude N19°.54, at the night time when the system is stable (between about 8 p.m. and 8 a.m.), and during the main observing period between April and August in 2007. Several cluster catalogs are compiled and studied for the expected SZE flux at AMiBA frequency, including OVRO (30 GHz; Mason et al. 2001), OVRO/BIMA (30 GHz; Grego et al. 2001; Reese et al. 2002), VSA (34 GHz; Lancaster et al. 2005), and SuZIE II (145, 221, and 355 GHz; Benson et al. 2004). The redshift range of $z \lesssim 0.3$ is so chosen that massive clusters of a typical virial radius of few Mpc is resolvable by AMiBA, whose resolution (6′) corresponds to a physical scale of 1.6 Mpc at $z = 0.3$ in a flat ΛCDM cosmology with matter density parameter $\Omega_{\rm m} = 0.3$, cosmological constant density parameter $\Omega_\Lambda = 0.7$, and Hubble constant $H_0 = 70$ km s^{-1} Mpc^{-1}. Among these six clusters, only A1689 and A2390 are known to have relaxed with a nearly isothermal profile. A1689 has a regular morphology in X-ray while A2390 is elongated. A2163, by contrast, is a merger with shocks and high-temperature regions, and A2142 is a merger with a strong frontal structure.

Due to the missing flux problem, most studies for the scientific implications of our results require the assistance of X-ray-derived properties of the clusters. In Table 2, we summarize the critical X-ray-derived parameters for the AMiBA clusters, which will be used by our companion science papers (Huang et al. 2009; Koch et al. 2009b; Liu et al. 2009; Umetsu et al. 2009). The X-ray temperatures are from Reese et al. (2002) for A2163, A2261, A1689, and A1995, from Markevitch et al. (1998) for A2142, and from Allen (2000) for A2390. The power-law index β in the isothermal β-model and the core radius θ_c are from Reese et al. (2002) for A2163, A2261, A1689, and A1995, from Sanderson & Ponman (2003) for A2142, and from Böhringer et al. (1998) for A2390. The X-ray core radii are mostly below 1 arcmin except for A2142 and A2163. These parameters are mostly X-emission weighted but not corrected for any cooling flows, which we further discuss in some science

Table 2
Parameters of AMiBA Clusters Derived from X-Ray Observations

Cluster	z	kT_X (keV)	β	θ_c (arcsec)
A1689	0.183	$9.66\pm^{0.22}_{0.20}$	$0.609\pm^{0.005}_{0.005}$	$26.6\pm^{0.7}_{0.7}$
A1995	0.322	$8.59\pm^{0.86}_{0.67}$	$0.770\pm^{0.117}_{0.063}$	$38.9\pm^{6.9}_{4.3}$
A2142	0.091	$9.7\pm^{1.5}_{1.1}$	$0.74\pm^{0.01}_{0.01}$	$188.4\pm^{13.2}_{13.2}$
A2163	0.202	$12.2\pm^{1.1}_{0.7}$	$0.674\pm^{0.011}_{0.008}$	$87.5\pm^{2.5}_{2.0}$
A2261	0.224	$8.82\pm^{0.37}_{0.32}$	$0.516\pm^{0.014}_{0.013}$	$15.7\pm^{1.2}_{1.1}$
A2390	0.232	$10.13\pm^{1.22}_{0.99}$	0.6	28.0

analyses such as the estimation of the Hubble constant H_0 (Koch et al. 2009b).

4. ANALYSIS METHOD AND RESULTS

We describe the formalism that we use to analyze AMiBA data from their raw format to the calibrated visibilities, images, and cluster profiles. AMiBA operates with a bandwidth of 16 GHz centered at 94 GHz. Its four-lag correlators provide two passbands of 8 GHz processing dual-linear polarizations. The challenge for the analysis of such data arises because the measured output of the instrument is not visibilities and because there are only two channels of wide bands causing considerable band-smearing effect in frequency. With the formalism presented here we successfully used the Sun to calibrate the image of Jupiter, and then used several planets (Jupiter, Saturn, Mars, Venus) to cross-calibrate. Jupiter was chosen as the primary calibrator for our science results.

When we observe a general source field $S(\mathbf{x})$ with a synthesized primary beam $B(\mathbf{x})$, the visibility along a baseline b of length L^b is

$$v^b(f) = \widetilde{S}(\mathbf{k}) \otimes \widetilde{B}(\mathbf{k}), \tag{4}$$

where $\mathbf{k}$ is the corresponding u–v mode, $f = |\mathbf{k}|c/(2\pi L^b)$ is the observing frequency, a tilde denotes the Fourier transform of a quantity, and $\otimes$ denotes a convolution. The four-lag outputs of a correlator for the source field can thus be modeled as

$$c^b(\tau_m) = \Re\left\{\int_{f_1}^{f_2} v^b(f) R^b(f) \times \exp\left[2\pi(f - f_0)\tau_m i + \phi^b(f) i\right] df\right\}, \tag{5}$$

where τ_m ($m = 1$–4) is the time delay for each of the four lags, $R^b(f)$ and $\phi^b(f)$ are the instrumental frequency-dependent gain and phase responses, respectively, f_0 is the frequency of the local oscillator (86 GHz), and f_1 and f_2 indicate the upper and lower ends of the response frequency range, i.e., $[f_1, f_2] = [86, 102]$ GHz for AMiBA. Our analysis must invert Equation (5) to obtain the calibrated visibilities $v^b(f)$.

Figure 5 shows our first-light lag data $c^b(\tau_m)$ of a drift scan on Jupiter. The fringing rate is determined by the angle between a baseline and the drift direction.

4.1. Time-Domain Preprocessing

Initially, the cluster data must be processed to remove baselines for which the system is malfunctioning. In addition to checking the instrumental logs of receivers and correlators, nightly drift-scan data for Jupiter or Saturn are used to identify obvious problems. We then apply Kolmogorov–Smirnov (K–S) test to filter out data sets for which the noise appears non-Gaussian (Nishioka et al. 2009). In the K–S test, a 5% significance level is used throughout and shown to be efficient in identifying data sets with known hardware problems. Finally, we remove periods of data where occasional mount control problems appear.

After this flagging, we difference the tracking data $c^b(\tau_m; t)$ in the two-patch observation in order to remove ground pickup and the electronic DC offset. 4σ outliers in the temporal domain are clipped before the differenced tracking data are integrated over the 3 minutes (4 minutes for the calibration) tracking period to yield the lag data $c^b(\tau_m) \equiv \langle c^b(\tau_m; t)\rangle_t$. Thus, each two-patch observation yields a set of four lags $c^b(\tau_m)$ ($m = 1$–4). We carefully verified that the noise of the lag data is white within the timescale of 10 minutes, assuring the scaling of the noise level with the two-patch integration time (Nishioka et al. 2009).

Further flagging of 4σ outliers is applied in the visibility space (see Section 4.3). Table 3 shows the percentages of data that are flagged out by each step. On average the fraction of good data is about 60%.

4.2. Lag-to-Visibility Transform

We must invert Equation (5) to convert the four lags $c^b(\tau_m)$ to two visibilities $v^b(f)$. Ideally, if $\tau_m \equiv \tau$ is continuous, then we need only perform an inverse Fourier transform from the τ domain to the f domain. However, τ here is sampled discretely, and conservation of the degrees of freedom provided by four-lag measurements implies that we can obtain at best two uncorrelated complex visibilities, with no redundancy.

We perform the inversion first by dividing the 16 GHz frequency band into two, $[f_1, f_d]$ and $[f_d, f_2]$, each associated with one "band visibility", and define a "visibility vector" as

$$\mathbf{v}^b = \begin{bmatrix} \Re\{v^b([f_1, f_d])\} \\ \Im\{v^b([f_1, f_d])\} \\ \Re\{v^b([f_d, f_2])\} \\ \Im\{v^b([f_d, f_2])\} \end{bmatrix}. \tag{6}$$

If we also write the four lags in column-vector form $\mathbf{c}^b \equiv c^b(\tau_m)$ ($m = 1$–4), then the visibility-to-lag transform resulted from Equation (5) is simply $\mathbf{c}^b = \mathbf{U}^b\mathbf{v}^b$, where $\mathbf{U}^b$ is a 4×4 matrix. The four columns in $\mathbf{U}^b$ can easily be obtained from Equation (5) as the four vectors $\mathbf{c}^b$ when setting each component in $\mathbf{v}^b$ to unity in turn while zeroing the other three components. Subsequently, the inversion is

$$\mathbf{v}^b = [\mathbf{U}^b]^{-1}\mathbf{c}^b = \mathbf{V}^b\mathbf{c}^b. \tag{7}$$

Once given any lag data $\mathbf{c}^b$, we can use Equation (7) to construct the band visibilities $v^b([f_1, f_d])$ and $v^b([f_d, f_2])$.

In principle, if $R^b(f)$ and $\phi^b(f)$ are accurately known, then $\mathbf{V}^b$ can be accurately determined so that there is no need for further calibration. However, in reality $R^b(f)$ and $\phi^b(f)$ are time dependent so that $\mathbf{V}^b$ is also time dependent and thus needs to be calibrated for every observation. Because the transform (Equation (7)) is linear, any reasonable choice of f_d, $R^b(f)$ and $\phi^b(f)$ should yield the same $\mathbf{v}^b$ after calibration. Hence, we make the simplest choice $f_d = (f_1 + f_2)/2 = 94$ GHz, $R^b(f) = 1$, and $\phi^b(f) = 0$, and then calibrate the data using the formalism described in Section 4.3. This choice makes the inversion (Equation (7)) exactly a discrete inverse Fourier transform that accounts for the band-smearing effect. An alternative, and equally natural, choice might be to have

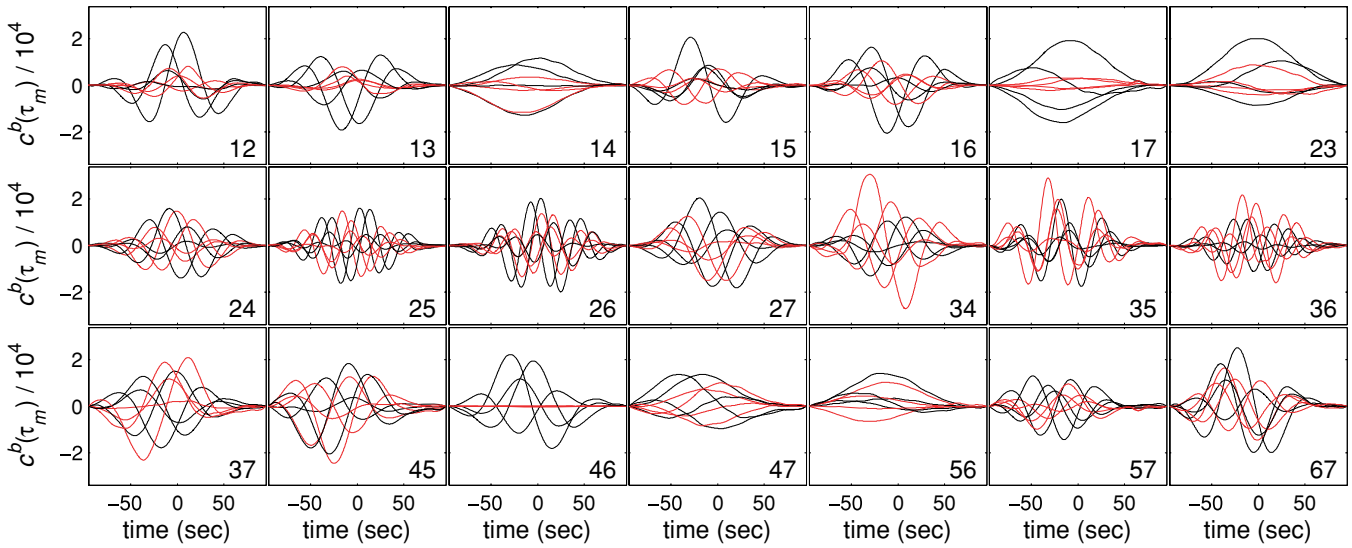

Figure 5. First-light lag data $c^b(\tau_m)$ of a drift scan on Jupiter in 2006 September. Each panel represents one baseline, with an "XY" label at the bottom-right corner indicating the correlation between the antennae X and Y. $X = 1$ represents the central antenna, with the other six close-packed around it. In each panel, the four black curves and four red curves correspond to the lag outputs of the LL and RR cross-polarization modes, respectively (see Section 2). Here, a low-pass filtering at 0.05 Hz is used to remove high-frequency noise. The horizontal time axis is the offset relative to the transit time.

equal power in the two frequency bands, with f_d so chosen that $\int_{f_1}^{f_d} R^b(f)df = \int_{f_d}^{f_2} R^b(f)df$, but this is difficult to implement since $R^b(f)$ is time dependent.

4.3. Calibration

For calibration, we observe planets using the same two-patch observing strategy (Section 3.4), the same time-domain preprocessing (Section 4.1), and the same lag-to-visibility transform (Equation (7), Section 4.2). The underlying band visibilities of these calibrators have the form

$$\mathbf{v}_*^{b(\mathrm{thy})} = \begin{bmatrix} M_1 \\ 0 \\ M_2 \\ 0 \end{bmatrix}, \tag{8}$$

where M_1 and M_2 are real constants, corresponding to the fluxes at different frequencies. However, the band visibilities constructed from observational data using Equation (7), where we have chosen $R^b(f) = 1$ and $\phi^b(f) = 0$, will take the form

$$\mathbf{v}_*^{b(\mathrm{obs})} = \begin{bmatrix} M_1^{b(\mathrm{obs})} \cos\phi_1^{b(\mathrm{obs})} \\ M_1^{b(\mathrm{obs})} \sin\phi_1^{b(\mathrm{obs})} \\ M_2^{b(\mathrm{obs})} \cos\phi_2^{b(\mathrm{obs})} \\ M_2^{b(\mathrm{obs})} \sin\phi_2^{b(\mathrm{obs})} \end{bmatrix}. \tag{9}$$

Since the involved operations are linear, there must exist a calibration matrix $\mathbf{C}^b$ that corrects this discrepancy, i.e.,

$$\mathbf{v}_*^{b(\mathrm{thy})} = \mathbf{C}^b \mathbf{v}_*^{b(\mathrm{obs})}. \tag{10}$$

We may model $\mathbf{C}^b$ as

$$\mathbf{C}^b = \begin{bmatrix} a_1^b \cos\phi_1^b & -a_1^b \sin\phi_1^b & 0 & 0 \\ a_1^b \sin\phi_1^b & a_1^b \cos\phi_1^b & 0 & 0 \\ 0 & 0 & a_2^b \cos\phi_2^b & -a_2^b \sin\phi_2^b \\ 0 & 0 & a_2^b \sin\phi_2^b & a_2^b \cos\phi_2^b \end{bmatrix}, \tag{11}$$

Table 3
Percentages of Data Flagged by Each Flagging Step

Cluster	Baseline Problems	Non-Gaussian Noise	Mount Problems	4σ Outliers	Good Data
A1689	2	11	4	2	81
A1995	35	4	5	21	35
A2142	8	15	1	2	74
A2163	7	8	1	1	83
A2261	25	1	1	27	46
A2390	5	16	3	7	69

where the parameters a_i^b and ϕ_i^b account for the gain and phase corrections relevant to the effects from $R^b(f)$ and $\phi^b(f)$ in Equation (5), respectively. By comparing the moduli and phases of $v_*^{b(\mathrm{thy})}$ and $v_*^{b(\mathrm{obs})}$, we obtain

$$\begin{aligned} a_1^b &= M_1/M_1^{b(\mathrm{obs})}, \quad a_2^b = M_2/M_2^{b(\mathrm{obs})}, \\ \phi_1^b &= -\phi_1^{b(\mathrm{obs})}, \quad \phi_2^b = -\phi_2^{b(\mathrm{obs})}. \end{aligned} \tag{12}$$

Finally, for a set of observed lag data $\mathbf{c}^b$, the calibrated band-visibility vector is

$$\mathbf{v}^b = \mathbf{C}^b \mathbf{V}^b \mathbf{c}^b. \tag{13}$$

We emphasize that this is a linear transform, so different initial choices for $R^b(f)$ and $\phi^b(f)$ that generate different $\mathbf{V}^b$ should lead to different $\mathbf{C}^b$ but the same final calibrated band visibilities $\mathbf{v}^b$. For each two-patch observation, we obtain one $\mathbf{v}^b$ for each cross-polarization mode and each baseline. For each baseline and each day, 4σ outliers in $|\mathbf{v}^b|$ are flagged.

4.4. Noise Estimation

In further analyses such as image making and model fitting for the cluster profile, a reliable estimate for the error in the band visibilities derived above will be needed. First, the two-patch differenced lag data $\mathbf{c}^b(t) \equiv c^b(\tau_m; t)$ are modeled as the linear sum of the signal and noise, $\mathbf{c}^b(t) = \mathbf{s}_c^b(t) + \mathbf{n}_c^b(t)$. Since such data for clusters are dominated by electronic noise (i.e., $\mathbf{n}_c^b(t) \gg \mathbf{s}_c^b(t)$) and the noise is white (Nishioka et al.

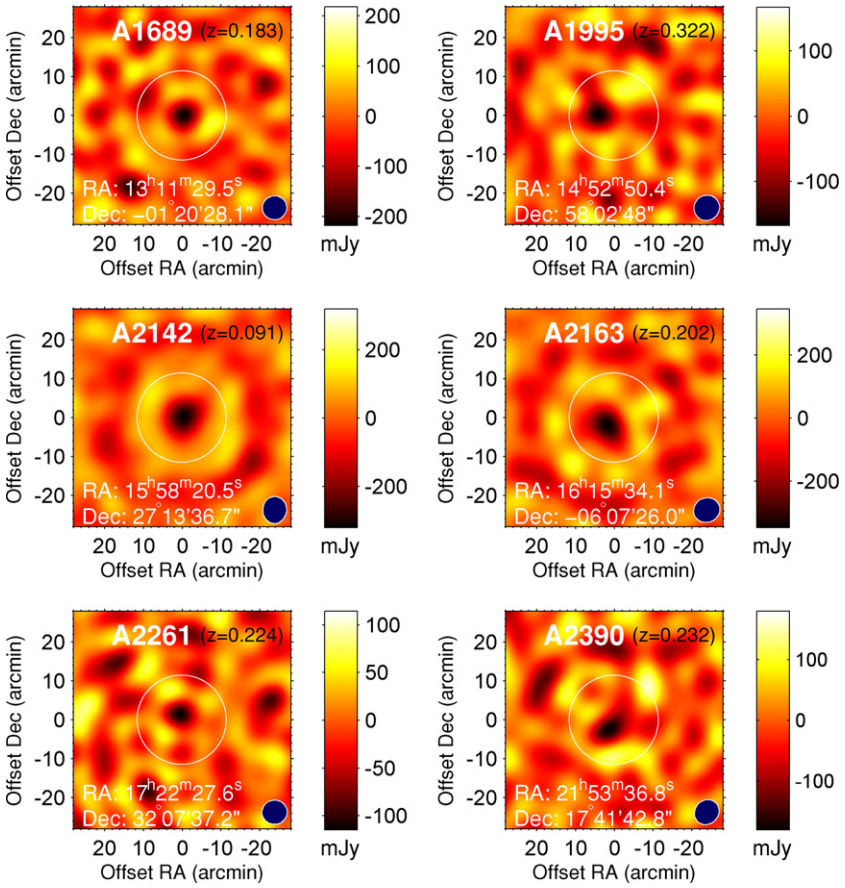

Figure 6. Dirty images of the six SZE clusters observed by AMiBA. The white circles indicate the half-maximum contour of the primary beam (the field of view; 23′), while the blue regions at the bottom-right corners indicate the half-maximum regions of the noise-weighted synthesized beams (∼ 6′). The central decrements in the flux density within the field of view provide strong evidence for the detections of SZE clusters.

2009), the noise variance associated with each time-integrated $\mathbf{c}^b \equiv \langle \mathbf{c}^b(t) \rangle_t$ can be directly estimated as

$$\left(\sigma_c^b\right)^2 \equiv \left\langle \left[\mathbf{n}_c^b\right]^2 \right\rangle \equiv \left\langle \left\langle \mathbf{n}_c^b(t) \right\rangle_t^2 \right\rangle \approx \frac{\langle [\mathbf{c}^b(t)]^2 \rangle_t}{\#_t}, \quad (14)$$

where $\#_t$ is the number of temporal data in the time integration. Then $(\sigma_c^b)^2$ constitutes the diagonal elements of the lag–lag noise correlation matrix $\mathbf{N}_c^b \equiv \langle \mathbf{n}_c^b \mathbf{n}_c^{b\mathrm{T}} \rangle$. The off-diagonal elements are found to be less than 10% of the diagonal elements (Nishioka et al. 2009) so we approximate them as zeros.

In a similar fashion, the band visibility obtained from Equation (13) can be modeled as a linear sum of the signal and noise, $\mathbf{v}^b(t) = \mathbf{s}_v^b(t) + \mathbf{n}_v^b(t)$. Finally, the noise correlation matrix for the calibrated band visibilities is

$$\mathbf{N}_v^b \equiv \left\langle \mathbf{n}_v^b \mathbf{n}_v^{b\mathrm{T}} \right\rangle \approx \mathbf{C}^b \mathbf{V}^b \mathbf{N}_c^b \mathbf{V}^{b\mathrm{T}} \mathbf{C}^{b\mathrm{T}}. \quad (15)$$

4.5. Image Making and Cleaning

We construct the "dirty" image of a cluster by making a continuous inverse Fourier transform of all the band visibilities from all days and all baselines, with noise weighting based on the noise variance. The instantaneous u–v coverage is improved in AMiBA operation by rotating the platform to eight polarization angles, giving a uniform angular interval of 7°.5 between sampled u–v modes $\mathbf{k}$ (see Section 3.2). Figure 6 shows the dirty images of these clusters. The flux decrement at the center of each target is evident, as expected for the SZE signal at the AMiBA center frequency of 94 GHz (see Section 2). The left part of Table 4 summarizes the angular sizes (azimuthally averaged FWHM) and the peak fluxes directly measured from these images.

Table 4
Properties of AMiBA SZE Images

Cluster	Dirty Images		Cleaned Images			
	Size	Flux (mJy)	Size	Flux (mJy)	S/N Ratio	Scale (Mpc)
A1689	(6.′1)	−217	(5.′7)	−168	6.0	(1.05)
A1995	(6.′8)	−167	(6.′8)	−161	6.4	(1.91)
A2142	7.′7	−320	9.′0	−316	13.7	0.92
A2163	7.′8	−347	11.′2	−346	11.7	2.24
A2261	(6.′2)	−115	(5.′8)	−90	5.2	(1.25)
A2390	7.′4	−180	8.′0	−158	6.6	1.78

Notes. Basic properties measured from the dirty and cleaned SZE images, including the angular sizes (azimuthally averaged FWHM), the peak flux, and the S/N ratios. For cleaned images, the peak flux is corrected for the attenuation by the primary beam due to an offset to the pointing center. The last column "scale" indicates the physical scale at z (see Table 2) corresponding to the angular size shown in the fourth column. Here, we have assumed a flat ΛCDM cosmology with $\Omega_m = 0.3$, $\Omega_\Lambda = 0.7$, and $H_0 = 70$ km s^{-1} Mpc^{-1}. The brackets indicate that the cluster appears unresolved in the SZE image.

A dirty beam for each cluster data set is constructed using the same method, and the dirty image and dirty beam are then processed by a CLEAN procedure (Hogbom 1974) in MIRIAD (MIRIAD-ATNF 2008) to yield a cleaned image. Figure 7 shows

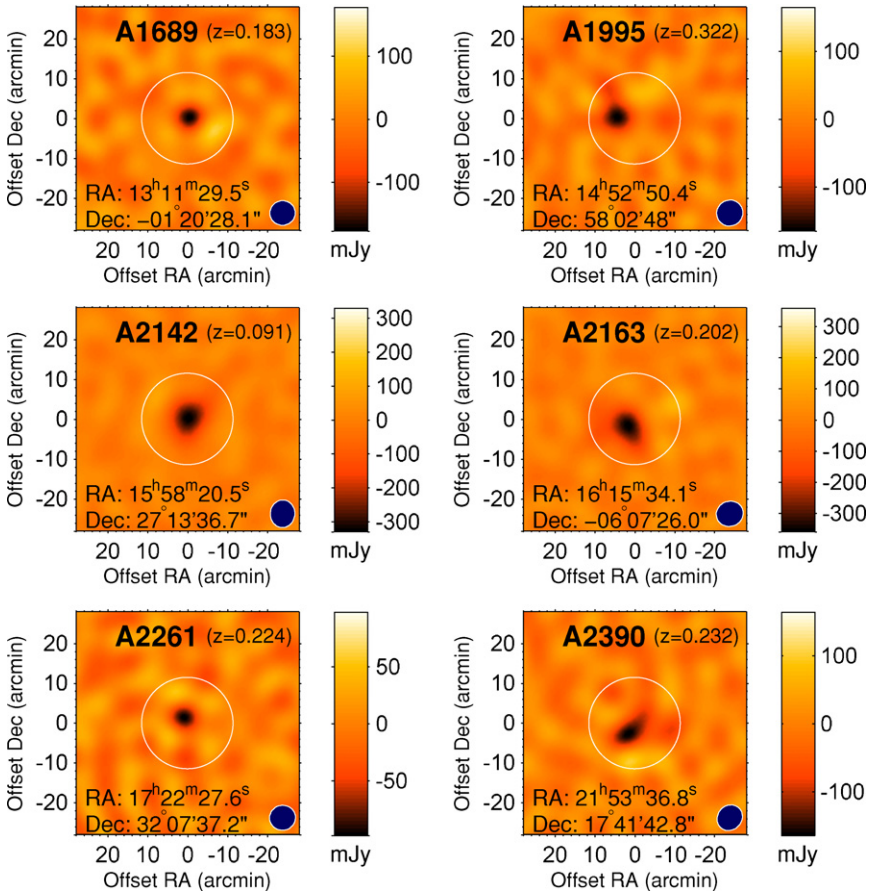

Figure 7. Cleaned SZE images of clusters observed by seven-element AMiBA. The white circles indicate the half-maximum contour of the primary beam (the field of view; 23′), and the blue patches at the bottom-right corners show the half-maximum regions of the dirty beams (∼ 6′).

the cleaned SZE images of the six AMiBA clusters, where the cleaned regions are indicated by the white circles, which are the FWHM contour of the primary beam. This process significantly reduces the convolution effects from the finite *u*–*v* coverage. The basic properties measured from the cleaned images are summarized in the right part of Table 4. The apparent angular sizes, as compared with the synthesized resolution of about 6′, indicate that we have partially resolved clusters A2142, A2163, and A2390, while A1689, A1995, and A2261 appear unresolved in these images. The SZE signals observed here are at the level of few hundred mJy, indeed consistent with the theoretical expectation $\Delta I_{\rm SZE} \sim -200$ mJy as discussed in Section 2.

In Table 4, the signal-to-noise (S/N) ratios are computed as the peak flux of the cleaned model (uncorrected for the primary beam attenuation) divided by the rms of the noise residual map. We note that the noise level in these results are dominated by the instrumental noise, leading to the fact that the scaling among the peak flux, S/N ratios, and integration time is consistent with the noise equivalent flux (point-source sensitivity) of 63 mJy $\rm hr^{-1/2}$ for the on-source integration time in a two-patch observation (Lin et al. 2009), i.e., for a 2-hr observation, 1 hr per patch, the noise rms is 63 mJy. Simulations also show that our analysis method (described in Section 4.2–4.4) does not bias the SZE amplitude but induces a statistical error at the few-percent level. The calibration error is controlled within 5% (Lin et al. 2009). The systematic effect from CMB anisotropy is estimated to be at a similar level as the instrumental noise, and the point-source contamination causes an underestimate of the SZE amplitude by about 10% (Liu et al. 2009).

4.6. Estimation of Cluster Profiles

It is useful for science purposes to estimate parameters describing the structures of the SZE clusters from the visibilities. We employ a maximum-likelihood analysis to estimate the band visibilities taking the priors that all the visibilities represent the same circularly symmetric source and that the visibility moduli within a frequency band are constant. Thus, there are only six nonredundant band visibilities $\{v_p;\ p = 1\text{–}6\}$ of six multipole bands corresponding to the two frequency bands $[f_1^n, f_2^n]$ $(n = 1, 2)$ of three baselines lengths (see Section 3.2 and Table 5), i.e., the observed band visibilities are modeled as

$$v^b\left(\left[f_1^n, f_2^n\right]|\{v_p\}, \mathbf{x}_0\right) = B(\mathbf{x}_0 - \mathbf{x}_1) v_{p(\in b,n)} \times \frac{1}{k_2^n - k_1^n} \int_{\mathbf{k}_1^n}^{\mathbf{k}_2^n} e^{i\mathbf{k}(\mathbf{x}_0 - \mathbf{x}_1)} d\mathbf{k}, \quad (16)$$

where $\mathbf{x}_0$ is the SZE cluster center, $\mathbf{x}_1$ is the pointing direction, $B(\mathbf{x})$ is the primary beam, and the integration accounts for the frequency band-smearing effect. These $\{v_p\}$ are equivalent to the band visibilities at $\mathbf{x}_1 = \mathbf{x}_0$ and therefore are real numbers. They indicate the cluster profile in the visibility space.

The Markov chain Monte Carlo (MCMC) approach with Metropolis–Hastings sampling is used for this eight-dimensional likelihood analysis. For each cluster three MCMC chains of 200,000 samples are used. The results are given in Table 5 and Figure 8. For all clusters the expected SZE decrement in the flux density is evident. We note that although the primary CMB makes a nonnegligible contribution to our observed visibilities (Liu et al. 2009), it appears with random

Table 5
SZE Centers and Visibility Profiles for AMiBA Clusters

Cluster	SZE Center $\mathbf{x}_0$ (J2000)		v_1 (mJy)	v_2 (mJy)	v_3 (mJy)	v_4 (mJy)	v_5 (mJy)	v_6 (mJy)
	R.A.	Decl.						
A1689	$13^h11.41 \pm 0.03^m$	$-1°20.7 \pm 0.'4$	-123 ± 92	-94 ± 89	-566 ± 109	-130 ± 108	-414 ± 185	85 ± 212
A1995	$14^h53.12 \pm 0.06^m$	$58°02.6 \pm 1.'0$	-234 ± 86	-106 ± 80	-241 ± 138	-207 ± 126	-53 ± 216	-32 ± 200
A2142	$15^h58.30 \pm 0.03^m$	$27°13.8 \pm 0.'5$	-508 ± 78	-366 ± 76	-140 ± 113	-205 ± 117	-9 ± 139	-206 ± 162
A2163	$16^h15.73 \pm 0.04^m$	$-6°09.5 \pm 0.'5$	-652 ± 110	-332 ± 113	93 ± 167	-236 ± 158	-457 ± 298	-31 ± 260
A2261	$17^h22.46 \pm 0.06^m$	$32°08.9 \pm 0.'5$	-34 ± 68	-108 ± 67	-160 ± 94	-78 ± 99	-412 ± 138	-37 ± 163
A2390	$21^h53.72 \pm 0.05^m$	$17°38.8 \pm 0.'7$	-148 ± 87	-185 ± 75	-260 ± 107	-273 ± 112	-96 ± 141	-44 ± 166

Notes. The maximum-likelihood results for the coordinates of SZE cluster centers $\mathbf{x}_0$ and band-visibility profiles $\{v_p\}$. The values v_1–v_6 correspond to the multipole bands of ℓ = [1092, 1193], [1193, 1295], [1891, 2067], [2067, 2243], [2184, 2387], [2387, 2590], respectively (see Sections 3.2, 4.6). v_1, v_3, v_5 correspond to the frequency band of [86, 94] GHz, and v_2, v_4, v_6 correspond to [94, 102] GHz. The three baseline lengths L^b are 0.606 m (for v_1, v_2), 1.05 m (for v_3, v_4), and 1.212 m (for v_5, v_6).

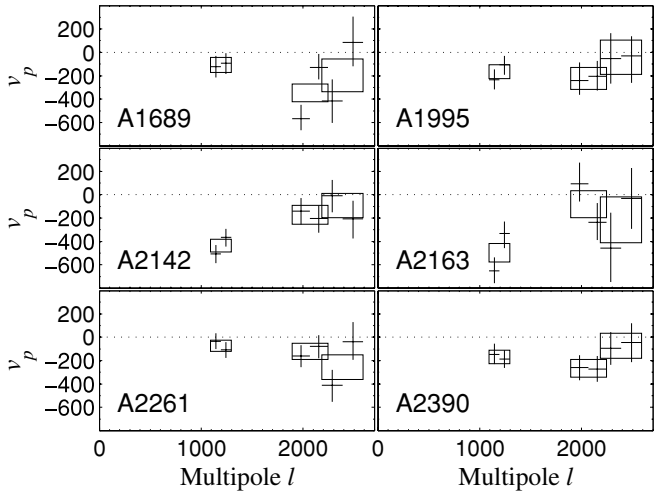

Figure 8. Visibility profiles $\{v_p\}$ of AMiBA SZE clusters. The data for the crosses are summarized in Table 5, while the boxes are the noise-weighted average of the two frequency bands at each baseline length.

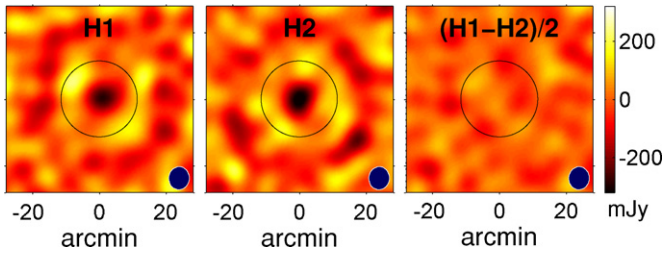

Figure 9. Both dirty images (left and middle) of A2142 analyzed from two equally divided subdata sets show a clear SZE signal of flux decrement, while their difference (right) indicates no recognizable signal but noise.

phase in u–v space and thus will not bias our analysis here but rather contribute as part of the error bars.

We emphasize that these results for $\{v_p\}$ and $\mathbf{x}_0$ are independent of cluster model. They can be further compared or combined with other experimental results, or fitted with a specific cluster model, for further study. The approach here is different from that in Liu et al. (2009), where an isothermal β-model is directly fitted with the visibilities to estimate the central brightness I_0, with the core radius θ_c and the power index β taken from X-ray analysis.

5. TESTS FOR SYSTEMATIC ERROR

To verify that our detections of SZE clusters are real rather than from the instrument or from the foreground, we implement several tests.

5.1. Differencing Maps

A commonly used powerful test is the so-called sum-and-difference test, where the temporal data are divided into two subsets of equal size and then processed separately. Figure 9 shows an example for A2142, where the two half-data images (left and middle) show a clear signal while their difference (right) reveals no signal but noise. Their average is very close to the overall dirty image shown in Figure 6. We have verified that such feature for the existence of signal is independent of the scheme for dividing the data into two halves. All data of the six clusters have passed this test.

5.2. Other Systematic Tests

We carried out several other tests for systematics. Long-duration (12 hr) observations of planets were used to check the stability of the system; an independent analysis path produced results for A2142 consistent to high accuracy with those presented here; and several two-patch blank-sky observations showed no signal above the expected CMB confusion (Lin et al. 2009). The noise properties of the lag data were investigated in detail indicating no systematics and no significant non-Gaussianity (Nishioka et al. 2009). The asymmetry of the antenna beams (Wu et al. 2001) was shown to be negligible. The pointing error is small enough that it has negligible effects on our results (Koch et al. 2009a), and the radio alignment was tuned to improve efficiency and tested for stability (J.-H. P. Wu et al. 2009, in preparation).

6. SCIENTIFIC IMPLICATIONS

The scientific implications of the AMiBA SZE results presented here are further studied by companion papers. The Hubble constant is estimated by first deriving the angular diameter distances of the clusters, and found to be $H_0 = 50^{+16+18}_{-16-23}$ km s^{-1} Mpc^{-1} (Koch et al. 2009b) in a flat ΛCDM cosmology with $\Omega_m = 0.3$ and $\Omega_\Lambda = 0.7$. We also estimate the integrated Compton parameter Y_{2500} (Huang et al. 2009), which is the Compton y parameter integrated out to the angular radius at which the mean overdensity of the cluster is equal to 2500 times the critical density of the universe at that redshift. Table 6 summarizes the results, as compared with the results from observations at 30 GHz (OVRO/BIMA, deduced from Morandi et al.

Table 6
Comparison of AMiBA SZE Results with Other Observations

Cluster	Y_{2500} ($\times 10^{-10}$ sr)		
	OVRO/BIMA	AMiBA	SuZIE II
A1689	2.17 ± 0.14	2.82 ± 0.86	$4.65^{+0.61}_{-0.51}$
A1995	0.71 ± 0.06	1.49 ± 0.58	...
A2142	...	13.44 ± 2.40	...
A2163	5.53 ± 0.41	6.61 ± 1.38	$5.50^{+0.76}_{-0.70}$
A2261	1.51 ± 0.18	1.72 ± 0.64	$4.46^{+1.70}_{-0.94}$
A2390	...	3.12 ± 0.98	$3.69^{+0.56}_{-0.57}$

Notes. The integrated Compton parameter Y_{2500} measured by AMiBA (86–102 GHz; Huang et al. 2009) as compared with results from OVRO/BIMA (30 GHz; deduced from Morandi et al. 2007, relativistic correction considered) and SuZIE II (145 GHz; deduced from Benson et al. 2004, relativistic correction considered).

2007, relativistic correction considered) and 145 GHz (SuZIE II, deduced from Benson et al. 2004, relativistic correction considered). Our results are consistent with those from OVRO/BIMA except for A1995, but seem to be systematically lower than those from SuZIE II. We also investigate the scaling relations between the Y_{2500} from AMiBA data and various X-ray-derived properties such as the gas temperature T_e, total mass M_{2500}, and luminosity L_x. The scaling powers of these relations are consistent with the predictions of the self-similar model (Huang et al. 2009). In the above studies, due to the missing flux problem the spherical isothermal β-model is used with the spectral index β and the core radius estimated by the X-ray data (see Table 2), and the normalization calibrated by the AMiBA SZE visibilities analyzed here (Liu et al. 2009).

We also perform a joint analysis of our SZE data with the weak gravitational lensing data from Subaru observations (Umetsu et al. 2009). For the four clusters of A1689, A2142, A2261, and A2390, the two data sets are found to be in great agreement in morphology. Quantitative analysis even yields an estimation for the baryonic fraction of $f_b(<r_{200}) = 0.133 \pm 0.027$ and concludes that when compared with the cosmic baryonic fraction $\Omega_b/\Omega_m = 0.171 \pm 0.009$ (Dunkley et al. 2009), $22\% \pm 16\%$ of the baryons are missing from the hot phase of clusters (Umetsu et al. 2009). The morphological agreement between our data and the lensing data and the consistency of f_b, H_0, Y_{2500} and scaling relations with literature are encouraging, indicating that AMiBA is a reliable CMB telescope.

7. CONCLUSION

We successfully detected six SZE clusters with the seven-element AMiBA in its compact configuration. The analysis method and results presented here mark a milestone for the AMiBA project and provides the first successful results for SZE clusters in the 3 mm band. These results are consistent with the published results based on data from other observations, and provide complementary information at the same time. A number of tests show that the system performs as expected from its design, and we anticipate that the current expansion to a 13-element system (Ho et al. 2008; Wu et al. 2008) will boost its capability for the study of CMB cosmology.

We thank the Ministry of Education, the National Science Council, the Academia Sinica, and National Taiwan University for their support of this project. We thank the Smithsonian Astrophysical Observatory for hosting the AMiBA project staff at the SMA Hilo Base Facility. We thank the NOAA for locating the AMiBA project on their site on Mauna Loa. We thank the Hawaiian people for allowing astronomers to work on their mountains in order to study the universe. This work is also supported by National Center for Theoretical Science, and Center for Theoretical Sciences, National Taiwan University for J.H.P.W. We are grateful for computing support from the National Center for High-Performance Computing, Taiwan. Support from the STFC for M.B. and K.L. is also acknowledged.

REFERENCES

Allen, S. W. 2000, MNRAS, 315, 269
Benson, B. A., et al. 2004, ApJ, 617, 829
Birkinshaw, M., & Lancaster, K. 2007, New Astron. Rev., 51, 346
Böehringer, H., et al. 1998, A&A, 334, 789
Chen, M.-T., et al. 2009, ApJ, 694, 1664
Dunkley, J., et al. 2009, ApJS, 180, 306
Grego, L., et al. 2001, ApJ, 552, 2
Halverson, N. W., et al. 2008, ApJ, submitted (arXiv:0807.4208)
Ho, P. T. P., et al. 2008, Mod. Phys. Lett. A, 23, 1243
Ho, P. T. P., et al. 2009, ApJ, 694, 1610
Hogbom, J. A. 1974, A&AS, 15, 417
Huang, C. W., et al. 2009, ApJ, submitted
Kneissl, R., et al. 2001, MNRAS, 328, 783
Koch, P., et al. 2006, in Proc. EuCAP ed. H. Lacoste & L. Ouwehand, (ESA SP-626), 668.1
Koch, P., et al. 2009a, ApJ, 694, 1670
Koch, P., et al. 2009b, ApJ, submitted
Kosowsky, A., et al. 2003, New Astron. Rev., 47, 939
Lancaster, K., et al. 2005, MNRAS, 359, 16
Lancaster, K., et al. 2007, MNRAS, 378, 673
LaRoque, S., et al. 2006, ApJ, 652, 917
Lin, K. Y., et al. 2004, ApJ, 608, L1
Lin, K. Y., et al. 2009, ApJ, 694, 1629
Liu, G. C., et al. 2009, ApJ, submitted
Markevitch, M., Forman, W. R., Sarazin, C. L., & Vikhlinin, A. 1998, ApJ, 503, 77
Mason, B. S., Myers, S. T., & Readhead, A. C. S. 2001, ApJ, 555, L11
MIRIAD-ATNF 2008, Australia Telescope National Facility http://www.atnf.csiro.au/computing/software/miriad/
Morandi, A., et al. 2007, MNRAS, 379, 518
Muchovej, S., et al. 2007, ApJ, 663, 708
Nishioka, H., et al. 2009, ApJ, 694, 1637
Readhead, A. C. S., et al. 2004, Science, 306, 836
Reese, E. D., Carlstrom, J. E., Joy, M., Mohr, J. J., Grego, L., & Holzapfel, W. L. 2002, ApJ, 581, 53
Ruhl, J., et al. 2004, Proc. SPIE, 5498, 11 (arXiv:astro-ph/0411122)
Sanderson, A. J. R., & Ponman, T. J. 2003, MNRAS, 345, 1241
Sunyaev, R. A., & Zeldovich, Y. B. 1972, Comm. Astrophys. Space Phys., 4, 173
Umetsu, K., et al. 2004, Mod. Phys. Lett. A, 19, 1027
Umetsu, K., et al. 2009, ApJ, 694, 1643
Wu, J.-H. P., et al. 2001, ApJS, 132, 1
Wu, J.-H. P., et al. 2004, Mod. Phys. Lett. A, 19, 1019
Wu, J.-H. P., et al. 2008, Mod. Phys. Lett. A, 23, 1675